ARTICLES

Production of J/ψ and $\psi(2S)$ mesons in π^-Be collisions at 515 GeV/c

A. Gribushin,[4] V. Abramov,[2] Yu. Antipov,[2] B. Baldin,[2] R. Crittenden,[4] C. Davis,[5] L. Dauwe,[6] S. Denisov,[2] A. Dyshkant,[2] A. Dzierba,[4] V. Glebov,[2] H. Goldberg,[3] R. Jesik,[3] V. Koreshev,[2] J. Krider,[1] A. Krinitsyn,[2] R. Li, [4] S. Margulies,[3,*] T. Marshall,[4] J. Martin,[4] H. Mendez,[3] A. Petrukhin,[2] J. Solomon,[3] V. Sirotenko,[2] P. Smith,[4] T. Sulanke,[4] R. Sulyaev,[2,*] F. Vaca,[3] and A. Ziemiński[4]

(E672 Collaboration)

S. Blusk,[12] C. Bromberg,[9] P. Chang,[10] B. Choudhary,[8] W. H. Chung,[12] L. de Barbaro,[13] W. Długosz,[10] J. Dunlea,[13] E. Engels, Jr.,[12] G. Fanourakis,[13] G. Ginther,[13] K. Hartman,[11] J. Huston,[9] V. Kapoor,[8] C. Lirakis,[10] S. Mani,[7] J. Mansour,[13] A. Maul,[9] R. Miller,[9] B. Y. Oh,[11] E. Pothier,[10] R. Roser,[13] P. Shepard,[12] D. Skow,[1] P. Slattery,[13] L. Sorrell,[9] W. Toothacker,[11] N. Varelas,[13] D. Weerasundara,[12] J. Whitmore,[11] C. Yosef,[9] and M. Zieliński[13]

(E706 Collaboration)

[1]*Fermi National Accelerator Laboratory, Batavia, Illinois 60510*
[2]*Institute for High Energy Physics, Serpukhov, Russia*
[3]*University of Illinois at Chicago, Chicago, Illinois 60607*
[4]*Indiana University, Bloomington, Indiana 47405*
[5]*University of Louisville, Louisville, Kentucky 40292*
[6]*University of Michigan at Flint, Flint, Michigan 48502*
[7]*University of California-Davis, Davis, California 95616*
[8]*University of Delhi, Delhi, India 110007*
[9]*Michigan State University, East Lansing, Michigan 48824*
[10]*Northeastern University, Boston, Massachusetts 02115*
[11]*Pennsylvania State University, University Park, Pennsylvania 16802*
[12]*University of Pittsburgh, Pittsburgh, Pennsylvania 15260*
[13]*University of Rochester, Rochester, New York 14627*
(Received 11 September 1995)

We have studied the production of J/ψ and $\psi(2S)$ charmonium mesons in 515 GeV/c π^-Be collisions in the Feynman-x range $0.1<x_F<0.8$. J/ψ mesons were detected via their decay into $\mu^+\mu^-$, and $\psi(2S)$ mesons were studied in both the $\mu^+\mu^-$ and $J/\psi\pi^+\pi^-$ decay modes. J/ψ differential cross sections have been measured as functions of x_F, p_T^2, and the cosine of the Gottfried-Jackson decay angle. We measure an inclusive J/ψ cross section of $B(J/\psi\rightarrow\mu^+\mu^-)\sigma(\pi^-\text{Be}\rightarrow J/\psi+X)/A=$ [9.3±0.1(stat)±1.1(syst)] nb/nucleon for J/ψ $x_F>0.1$. Our results are compared with those from other experiments performed at lower beam energies. We also measure the differential $\psi(2S)$ cross section as a function of both x_F and p_T^2, and a $\psi(2S)$ inclusive cross section of $B(\psi(2S)\rightarrow J/\psi\pi^+\pi^-)\sigma(\pi^-\text{Be}\rightarrow\psi(2S)+X)/A=$[7.4±1.5(stat)±1.2(syst)] nb/nucleon for $\psi(2S)$ $x_F>0.1$. The fraction of the inclusive J/ψ yield due to $\psi(2S)$ meson decays is 0.083±0.017(stat) ±0.013(syst), and the observed ratio of $\psi(2S)$ decay rates is $B(\psi(2S)\rightarrow J/\psi\pi^+\pi^-)/B(\psi(2S)\rightarrow\mu^+\mu^-)$ =30.2±7.2(stat)±6.8(syst). We have searched for production of ''hidden'' charm resonances decaying into either $J/\psi\pi^\pm, \psi(2S)\pi^\pm$, or $J/\psi\pi^+\pi^-$ systems, and report an upper limit of 3.1 nb/nucleon for the product of branching ratio and cross section for the recently reported enhancement at a $J/\psi\pi^+\pi^-$ mass of 3.836 GeV/c^2.

PACS number(s): 13.85.Ni, 25.40.Ve, 25.80.Ls

*Deceased.

I. INTRODUCTION

The hadronic production of charmonium states continues to play a role in the study of perturbative and nonperturbative quantum chromodynamics (QCD) [1,2]. A significant fraction of the J/ψ's produced in hadronic interactions come from the decay of higher-mass charmonium states. One of the goals of this experiment is measuring the cross section for the production of several charmonium states, $J/\psi, \psi(2S)$, and χ_c, and comparing these values to theoretical predictions using various models of parton and final-state interactions.

In addition to QCD studies, charmonium hadroproduction provides spectroscopic information complementary to that obtained in e^+e^- interactions. The initial states produced in hadronic collisions are not restricted to those with the quantum numbers of the photon, as in e^+e^- interactions.

In this paper, we report the J/ψ and $\psi(2S)$ total and differential inclusive cross sections, measurements of the fraction of the inclusive J/ψ yield due to $\psi(2S)$ decay, the ratio of the $\psi(2S)$ decay rates into $J/\psi\pi^+\pi^-$ and $\mu^+\mu^-$, and results of a search for ''hidden'' charm resonances decaying into either $J/\psi\pi^\pm, \psi(2S)\pi^\pm$, or $J/\psi\pi^+\pi^-$ systems. In a subsequent paper, we will discuss the cross sections for χ_c and direct J/ψ production, and will compare current models of QCD interactions to our results [3].

II. APPARATUS

The experiment was performed in the Fermilab Meson West beam line using a large-aperture, open-geometry spectrometer with the capability of studying high-mass muon pairs. The layout of the experiment is shown in Fig. 1. A brief description of the essential elements of the Meson West apparatus as implemented in the 1990 fixed target run follows.

The beam line included a 42-m-long differential Cherenkov counter capable of tagging incident beam particles. The unseparated negative secondary beam at 515 GeV/c was composed primarily of pions with a small admixture ($<5\%$) of kaons. The Cherenkov counter was not directly used in the dimuon analysis described in this paper. The beam intensity varied during the run, and at its maximum was 2×10^8 pions per 23s-long spill (at 57-s intervals).

A hadron shield consisting of 5 m of iron was located upstream of the target to reduce background from off-axis hadrons and soft muons. One scintillator veto wall was placed upstream of the hadron shield, and two others were located downstream of the shield. These veto walls were used to identify high-energy muons that penetrated the iron. An on-line veto for the dimuon trigger rejected events with coincidences between a signal from the upsteam veto wall and a signal from at least one of the downstream walls.

Incident beam was defined via three scintillation counters (BA, BB, and BH) located upstream of the target, and a three-plane (X,Y, and U) beam hadoscope with mm-scale resolution. A beam particle was identified by signals from the BA and BB counters plus at least a twofold coincidence from the beam hodoscope, and no signal from the BH counter, which had a 1-cm-diam hole centered on the beam. Signals from the beam hodoscope were also employed to veto events containing more than one spatially isolated beam particle. The redundancy in the beam trigger elements was used to satisfy simultaneously the different timing requirements of the dimuon triggers (of E672) and the high-p_T electromagnetic triggers (of E706).

The target consisted of two copper pieces, each 0.8 mm thick, followed by two pieces of beryllium, 3.71 cm and 1.12 cm thick, respectively, separated by 1 cm. The total thickness of the target material corresponded to 9% of a pion interaction length.

Three X-Y modules of silicon-strip detectors (SSD's) [4] were located upstream of the target to measure the trajectories of incident beam particles. Each module consisted of two single-sided planes. Five more X-Y SSD modules were located downstream of the target. These modules were used to determine the trajectories of charged particles produced in the target and to reconstruct primary and secondary vertices. The SSD's in the first downstream module had a 25-μm-pitch inner region and a 50-μm-pitch outer region; the SSD's in the other modules had 50-μm pitch throughout.

A dipole magnet producing a p_T impulse of 0.45 GeV/c was located downstream of the SSD's. Four proportional wire chamber (PWC) modules were located downstream of the dipole magnet. Each module contained four wire planes to provide X,Y,U, and V measurements. (The U and V coordinates were a pair of orthogonal coordinates rotated by 37° relative to the X and Y coordinates.) The wires in each plane had 2.54-mm pitch. An area of from 6 to 26 cm^2 in the

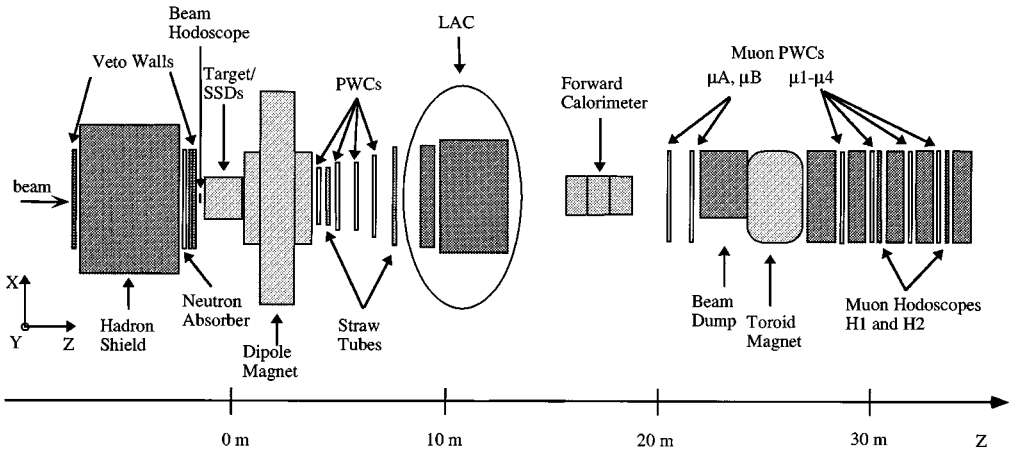

FIG. 1. Plan view of the Fermilab Meson West spectrometer during the 1990 fixed target run.

center of each plane had reduced sensitivity to provide protection against interacting beam particles. Two stations of straw tube drift chambers [5], each with four planes in the X and four planes in the Y directions, were located adjacent to the outside PWC modules. In the analysis reported here, momentum measurements for charged nonmuon tracks employed the SSD's, the dipole magnet, and the PWC's, yielding a momentum resolution of $\Delta p/p = 0.06\% p$.

Interactions were detected by a pair of scintillation counters located before the dipole magnet and another pair after the magnet. An interaction was defined as a signal from at least two of these counters in coincidence with a valid beam particle. The interaction rate was generally less than 0.8 MHz.

A liquid-argon calorimeter (LAC) [6] was located downstream of the magnetic spectrometer. The LAC contained both electromagnetic and hadronic sections. The outer radius of the electromagnetic section was 165 cm; the inner radius was 20 cm. A helium-gas-filled beam pipe was inserted along the axis of the LAC to minimize interactions of beam particles. The total LAC material corresponded to more than 10 interaction lengths. Approximately 70% of the muons recorded in the muon detector passed through the beam pipe.

An iron and scintillator forward calorimeter was located downstream of the LAC to detect particles passing through the beam pipe. The forward calorimeter had a diameter of 1 m with a 3-cm-diam axial beam hole and contained 10 absorption lengths of material.

The muon detector [7,8] was located 20 m downstream of the target and extended for 16 m. The detector contained, in sequence, two muon PWC stations (μA, μB) with four planes each (X, Y, U, and V), a beam dump consisting of tungsten and steel imbedded in concrete, an iron toroid magnet producing an average p_T impulse of 1.3 GeV/c, and four more PVC's, ($\mu 1 - \mu 4$), each with three planes (X, U, and V). In these PWC's, the U and V coordinates were at angles of 45° above and below the horizontal, respectively. Iron, lead, and concrete shielding was interspersed between chambers $\mu 1$ through $\mu 4$. Two muon hodoscope planes, $H1$ and $H2$ (each with 16 petal-shaped scintillation counters) were also located in this region. The outer radius of the muon chambers and hodoscopes was 135 cm. The acceptance of the muon spectrometer was limited by tapered axial holes, ranging from 13 to 20 cm in radius, through the toroid magnet, the muon chambers, and the scintillator hodoscopes. The hole in the toroid was filled with lead absorber.

The muon detector elements $H1$, $H2$, and $\mu 1 - \mu 4$ were shielded from hadrons by material in the LAC, the forward calorimeter, the beam dump, the toroid, and the concrete shielding. Muons produced at the target with energies larger than $\sim$15 GeV penetrated this material, and all particles reaching the muon hodoscopes were assumed to be muons. Two or more hits in each of the muon hodoscopes were required as part of the dimuon pretrigger [9]; the average hit multiplicity was 2.3 per hodoscope plane. In addition to the muon hodoscope requirement, signals from the upstream veto walls completed the pretrigger requirement. The pretrigger rate was 2×10^{-4} per live interaction. The pretrigger efficiency for two muons penetrating the system was 0.76 and remained constant during the data taking period. No radial dependence of the pretrigger counter efficiencies was observed.

The final dimuon trigger was formed by the dimuon trigger processor (DMTP), which reconstructed space points in PWC's $\mu 1$ and $\mu 4$, formed muon tracks (requiring an additional hit in either $\mu 2$ or $\mu 3$ along the projected track trajectory), measured muon momenta from the estimated bend in the toroid (assuming that the tracks originated in the target), and calculated the dimuon invariant mass. Trajectories of muon tracks reconstructed in the downstream muon PWC's were projected to the center of the target. The processor accepted only muon tracks with at least three hits in each of the μA and μB chambers within roads around the projected trajectory. A trigger resulted if any of the dimuon masses, calculated assuming massless muons, was above a preset threshold. A mass threshold of 0.7 GeV/c^2 resulted in a trigger rate of 2×10^{-5} per live interaction. The average DMTP processing time was 10 μs per pretrigger, which included 5 μs to decode the muon chamber data. The combined efficiency of the chambers and the DMTP algorithm was 0.77 for dimuon events. The DMTP mass resolution for the J/ψ was 550 MeV/c^2.

III. DATA

Approximately 5×10^6 dimuon triggers were recorded during the 1990 run (corresponding to a luminosity of 7.5 pb^{-1} per nucleon on Be). This yielded 3×10^5 events with reconstructed dimuon combinations originating from the target region. For each dimuon-triggered event, the muon tracks were linked through the entire detector. This fit accounted for multiple-scattering effects, and required consistency between the track momenta determined by the dipole and the toroid magnets. Only events with at least two fully linked muons were retained. The remaining track segments in the SSD's and upstream PWC's were used to reconstruct other tracks and find the event vertices. The distribution of the reconstructed primary vertices along the nominal beam (Z)

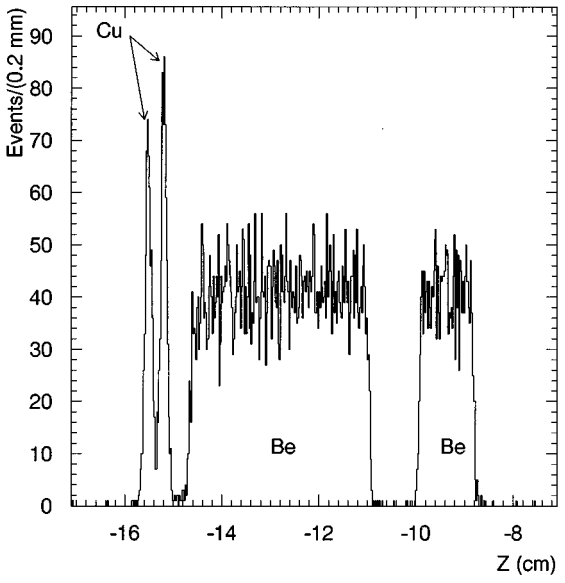

FIG. 2. Primary vertex Z-coordinate distribution for events containing dimuons with reconstructed masses in the J/ψ mass range.

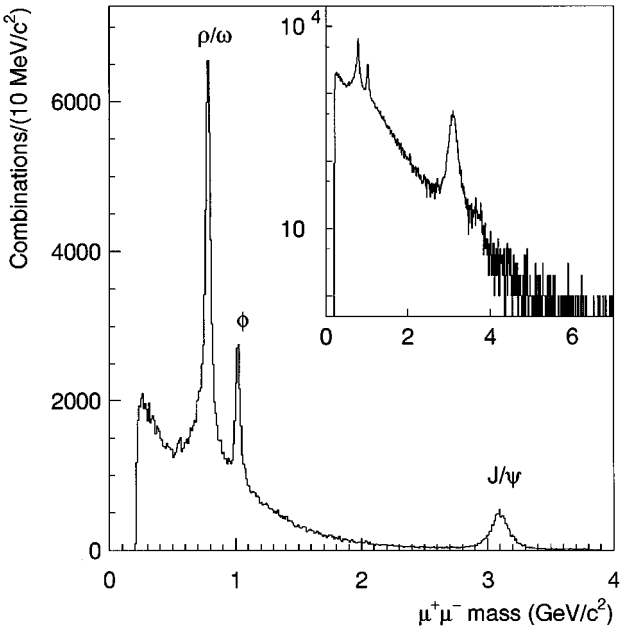

FIG. 3. The invariant mass distribution of $\mu^+\mu^-$ pairs produced in π^-Be interactions (data were collected with varying dimuon trigger processor mass thresholds). The inset displays the data in semilog form.

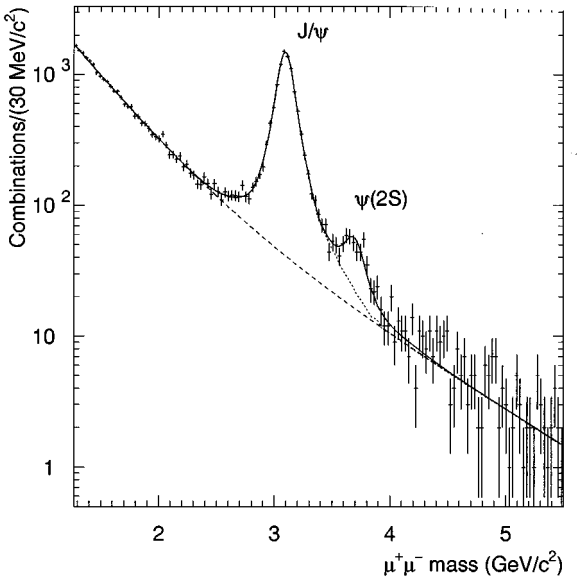

FIG. 4. The invariant mass distribution for $\mu^+\mu^-$ pairs in the J/ψ mass region. The solid curve is a fit to the data, the dashed curve shows the background contribution, and the dotted curve illustrates the background under the $\psi(2S)$ signal.

direction, for events containing reconstructed dimuons in the mass range 2.8 – 3.4 GeV/c^2, is shown in Fig. 2.

Dimuons contributing to this analysis came from events with primary vertices in the beryllium targets, and had dimuon Feynman-x ($x_F = 2p_z/\sqrt{s}$) in the range $0.1 < x_F < 0.8$. Figures 3 and 4 show the reconstructed opposite-sign dimuon invariant mass distributions for the full mass range and in the J/ψ region, respectively. A fit to the high-mass sample yields $9600 \pm 105(\text{stat}) \pm 200(\text{syst})$ J/ψ's with a full width at half maximum (FWHM) mass resolution of 160 MeV/c^2, and $270 \pm 35(\text{stat}) \pm 50(\text{syst})$ $\psi(2S)$'s. This fit used resolution functions for the J/ψ and $\psi(2S)$ resonances determined by Monte Carlo simulations, plus the sum of two exponentials for the continuum background. The J/ψ mass obtained from the fit is (3.0975±0.0003) GeV/c^2. The $\psi(2S)$ mass was fixed at the Particle Data Group value [10]. The systematic uncertainties in the number of J/ψ and $\psi(2S)$ events take into account variations in the shapes assumed for the signal and background distributions.

To determine overall reconstruction efficiencies and acceptances, we generated 3×10^5 Monte Carlo J/ψ events. The x_F and p_T^2 distributions of the generated Monte Carlo J/ψ's were taken from our previous measurement [8]. We assumed that J/ψ's decay isotropically (consistent with observations to be described in the next section). These Monte Carlo events also contained additional charged tracks with an average multiplicity consistent with the data. The dimuons and associated particles were propagated through a GEANT simulation of the Meson West spectrometer, which incorporated measured spectrometer chamber efficiencies and instrumental noise determined from our data. The dimuon events were then processed with the same tracking programs used for the data. We have evaluated the J/ψ reconstruction efficiency and geometrical acceptance as a function of three variables: (i) x_F, the J/ψ Feynman-x; (ii) p_T^2, the square of the J/ψ transverse momentum; and (iii) $\cos\theta$, the cosine of the Gottfried-Jackson decay angle between the μ^+ and the beam axis in the J/ψ rest frame. The product of acceptance and reconstruction efficiency, $a_{J/\psi\to\mu^+\mu^-} \cdot \varepsilon_{J/\psi\to\mu^+\mu^-}$, was calculated (a) as a two-dimensional surface over the x_F and p_T^2 plane (see Fig. 5), and (b) as one-dimensional distributions averaged over the other variable using an iterative technique [see Figs. 6(a) and 6(b)]. (In the second method, the input Monte Carlo x_F and p_T^2 distributions for a given iteration were weighted to match those of the data corrected by the acceptance and reconstructing efficiencies determined in the previous iteration. The iterations were stopped once stability was achieved.) The two methods gave consistent cross-section results. The product of acceptance and efficiency as a function of $\cos\theta$, integrated over the x_F and p_T^2 spectra, is shown in Fig. 6(c).

IV. J/ψ DIFFERENTIAL CROSS SECTIONS

J/ψ candidates consisted of opposite sign dimuons with invariant mass between 2.8 and 3.4 GeV/c^2 originating from the primary vertex. The background accounts for 8% of the combinations in the J/ψ mass range, and this fraction does not change appreciably as a function of x_F or p_T^2. Fits to the dimuon mass spectra, similar to the one described in Sec. III and shown in Fig. 4, for different regions of x_F and p_T^2 indicate that the variation in the background contribution is less than ±1% of the total number of combinations in the J/ψ mass region. With the constraints that the $\mu^+\mu^-$ invariant mass be 3.097 GeV/c^2, and that both muons come from the same vertex, a two-constraint kinematic fit was carried out for each J/ψ candidate to improve the muon momentum resolution. The resulting x_F resolution for fitted J/ψ's varied from 0.005 at $x_F = 0.2$ to 0.03 at $x_F = 0.7$. Because of this constrained fit and the observed background stability, we did

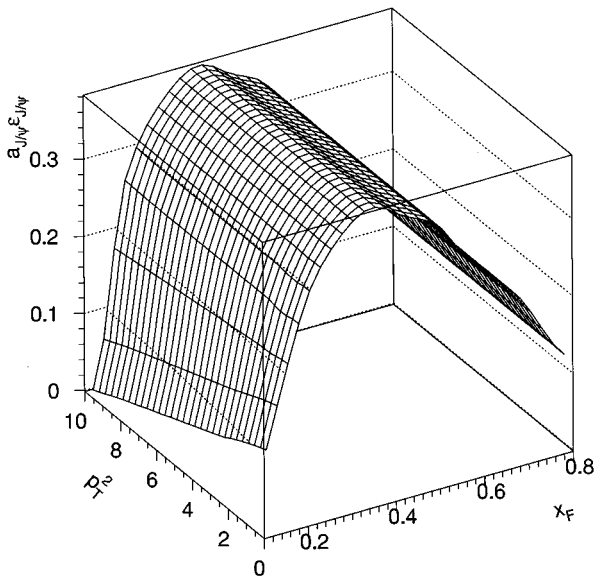

FIG. 5. Surface illustrating the product of geometrical acceptance and reconstruction efficiency as a function of x_F and p_T^2 for the $J/\psi\to\mu^+\mu^-$ decay.

not perform a bin-by-bin background subtraction to determine the J/ψ differential distributions, but instead normalized the distributions so that their integrals matched the background-subtracted J/ψ integrated cross section.

The J/ψ differential distributions with empirical fits are shown in Fig. 7, and tabulated in Table I. Data points were corrected for the geometrical acceptances and reconstruction efficiencies discussed in the previous section.

The Feynman-x acceptance of the apparatus does not permit an independent determination of the differential cross section behavior for $x_F<0.1$. We used the following parametrization to describe $d\sigma/dx_F$ [11] [see Fig. 7(a)]:

$$d\sigma/dx_F\propto x_1^a(1-x_1)^\kappa(1-x_2)^{\kappa+2}/(x_1+x_2), \qquad (4.1)$$

where

$$x_{1,2}=0.5[\sqrt{x_F{}^2+4\tau}\pm x_F], \qquad (4.2)$$

and $\tau=M_{J/\psi}^2/s$. Here, x_1 represents the beam parton fractional momentum and x_2 the target parton fractional momentum. The values obtained from the fit are $\kappa=2.19\pm0.10$ and $a=0.33\pm0.06$, with a χ^2 per degree of freedom, $\chi^2/N_{\rm DF}=30/32$. The empirical factor x_1^a in Eq. (4.1), which was not used in [11], was introduced to improve the fit in the low-x_F region. A fit with a set to zero gives $\kappa=1.69\pm0.04$ with $\chi^2/N_{\rm DF}=50/33$.

The p_T^2 spectrum [Fig. 7(b)] was fit to the empirical form [12]

$$d\sigma/dp_T^2\propto(1+p_T^2/\beta^2)^c \qquad (4.3)$$

with parameters $\beta=(2.3\pm0.2)$ GeV/c and $c=-4.7\pm0.6$ and $\chi^2/N_{\rm DF}=61.47$. Figure 8 shows that the measured average p_T of the J/ψ candidates, $\langle p_T\rangle$, is consistent with a slow decrease as a function of the J/ψ x_F. The x_F-integrated value $\langle p_T\rangle=(1.17\pm0.02)$ GeV/c measured

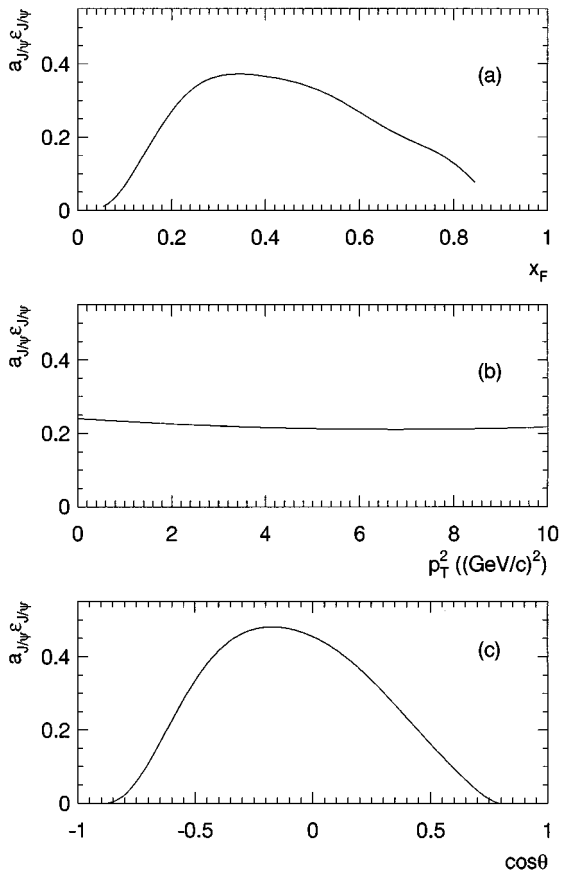

FIG. 6. Product of geometrical acceptance and reconstruction efficiency for the $J/\psi\to\mu^+\mu^-$ decay as a function of (a) x_F, (b) p_T^2, and (c) $\cos\theta$.

by this experiment is larger than the corresponding values reported at lower $\sqrt{s}$. As shown in Fig. 9, the value of $\langle p_T\rangle$ grows linearly with c.m. energy.

A fit to the $\cos\theta$ distribution in the range $|\cos\theta|<0.8$ [Fig. 7(c)] using the function

$$d\sigma/d(\cos\theta)\propto(1+\lambda\cos^2\theta) \qquad (4.4)$$

yields $\lambda=-0.01\pm0.08$ and $\chi^2/N_{\rm DF}=33/34$, which is consistent with unpolarized J/ψ production. Only 0.3% of the observed J/ψ's have $|\cos\theta|>0.8$.

V. J/ψ INTEGRATED CROSS SECTION

The inclusive J/ψ cross section was determined as follows:

$$B(J/\psi\to\mu^+\mu^-)\sigma(\pi^-\text{Be}\to J/\psi+X)/A=N_{J/\psi}^{(c)}/(Le_1e_2). \qquad (5.1)$$

Here, $N_{J/\psi}^{(c)}$ is the measured number of J/ψ's coming from primary vertices corrected for geometrical acceptance and reconstruction efficiency on an event-by-event basis (see Fig. 5), L is the integrated luminosity, e_1 is a luminosity correction factor, and e_2 is an apparatus efficiency factor.

The integrated luminosity was calculated from the total number of beam particles incident on the 8.92 g/cm^2 of beryllium during the live time of the spectrometer. The lumi-

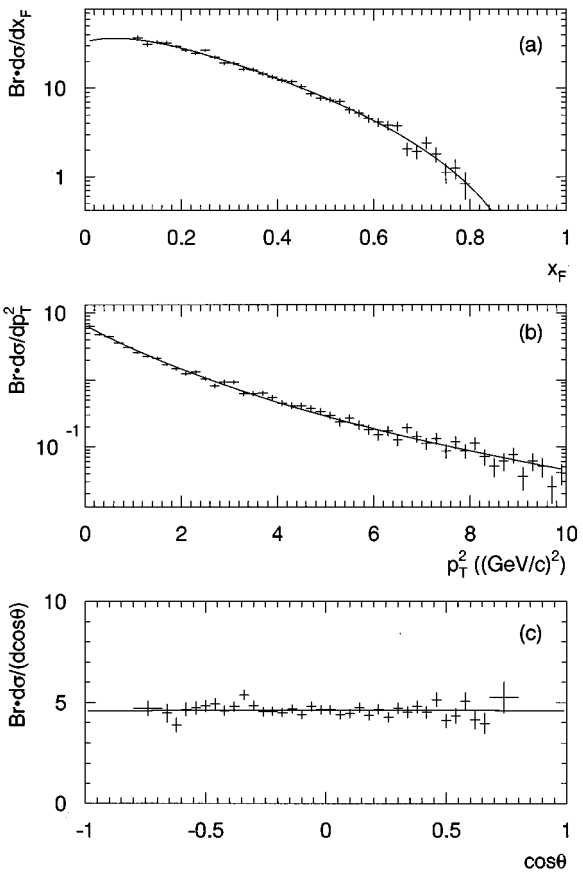

FIG. 7. Product of $B(J/\psi\rightarrow\mu^+\mu^-)$ and the J/ψ differential cross section as a function of (a) x_F (nb/nucleon), (b) p_T^2 [nb/nucleon/GeV/c)^2], and (c) $\cos\theta$ (nb/nucleon). The solid curves represent empirical fits to the data as described in the text (uncertainties are statistical only; the overall normalization uncertainty is $\pm 12\%$).

nosity correction factor, e_1, includes corrections for dimuon pretrigger and trigger processor dead time, losses due to timing requirements between the muon detector and the rest of the spectrometer, and transverse target fiducial cuts. The apparatus efficiency factor, e_2, was used to account for the pretrigger hodoscope and the dimuon trigger processor efficiencies mentioned in Sec. II.

The J/ψ cross section was evaluated for each of seven groups of data corresponding to different running conditions. The apparatus efficiency factor, $e_2=0.59\pm0.05$, remained constant during the data-taking period. The luminosity correction factor, e_1, varied from 0.61 to 0.96, with a weighted average $e_1=0.76$. The cross sections determined for the individual groups agree with each other within uncertainties, and the spread of the absolute values is less than 19%. A weighted average was used to determine the cross section reported.

For J/ψ mesons with $x_F>0.1$, we find

$$B(J/\psi\rightarrow\mu^+\mu^-)\sigma(\pi^-\mathrm{Be}\rightarrow J/\psi+X)/A$$
$$=[9.3\pm0.1(\mathrm{stat})\pm1.1(\mathrm{syst})]\quad \mathrm{nb/nucleon}.$$

The error quoted is dominated by systematic uncertainties in the luminosity, trigger, reconstruction efficiencies, and acceptance calculations. This result is consistent with our previous measurements [7,13,14].

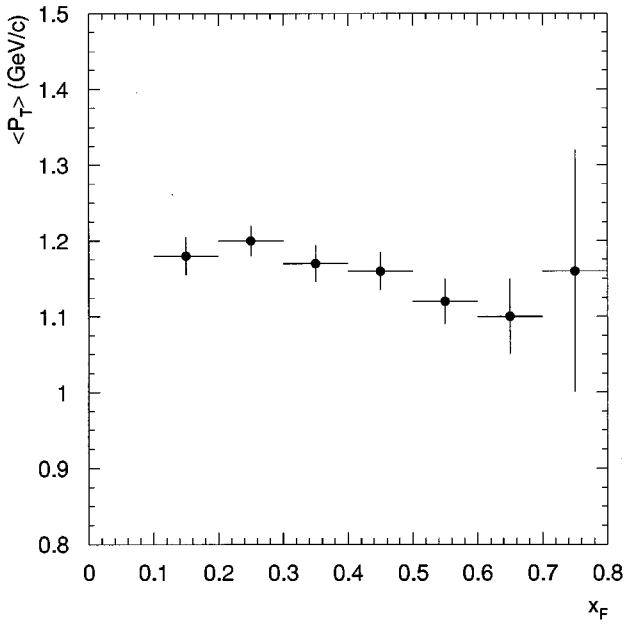

FIG. 8. The average J/ψ transverse momentum versus the $J/\psi x_F$ (uncertainties are statistical only).

For comparison with theory and with other experiments for which the data cover different kinematic regions, we use the results of the fit to Eq. (4.1) to determine the J/ψ cross section for the region $x_F>0$. The extrapolation factor required is 1.39 ± 0.05. The error quoted takes into account uncertainties in the x_F distribution at low x_F. The corresponding product of dimuon branching ratio and cross section is $[12.9\pm0.2(\mathrm{stat})\pm1.6(\mathrm{syst})]$ nb/nucleon for $x_F>0$. The

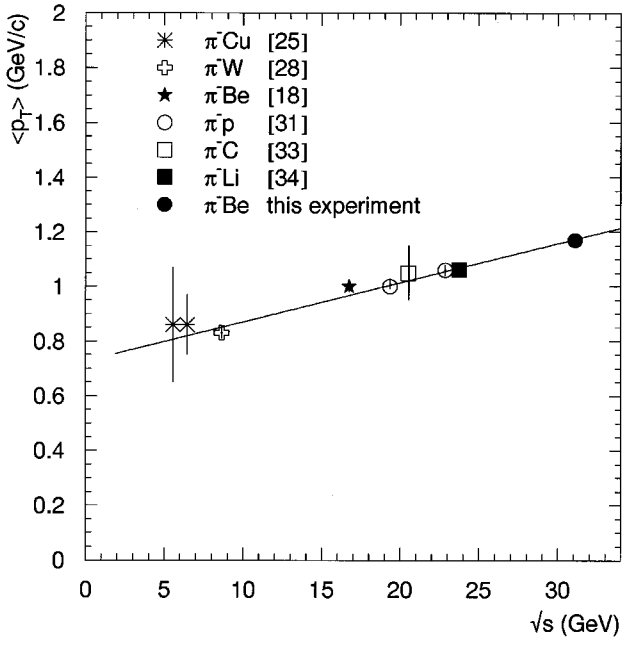

FIG. 9. Dependence of the average J/ψ transverse momentum on $\sqrt{s}$ for π^- nucleon interactions. The data are fitted with a linear function (uncertainties are statistical and systematic errors added in quadrature).

TABLE I. Differential cross sections for J/ψ production in 515 GeV/c π^-Be interactions. Quoted uncertainties reflect statistical errors only. The normalization uncertainty is ±12%.

x_F bin	$d\sigma/dx_F$ (nb/nucleon)	p_T^2 bin [(GeV/c)^2]	$d\sigma/dp_T^2$ [nb/nucleon/(GeV/c)^2]	$\cos\theta$ bin	$d\sigma/d\cos\theta$ (nb/nucleon)
		0.0–0.2	6.39 ± 0.17		
		0.2–0.4	4.82 ± 0.15		
		0.4–0.6	4.48 ± 0.14		
		0.6–0.8	3.60 ± 0.13		
		0.8–1.0	3.10 ± 0.12		
0.10–0.12	36.4 ± 2.4	1.0–1.2	2.59 ± 0.11	−0.80–−0.68	4.71 ± 0.37
0.12–0.14	31.3 ± 1.8	1.2–1.4	2.29 ± 0.10	−0.68–−0.64	4.47 ± 0.47
0.14–0.16	32.8 ± 1.6	1.4–1.6	2.13 ± 0.10	−0.64–−0.60	3.89 ± 0.37
0.16–0.18	32.3 ± 1.4	1.6–1.8	1.706 ± 0.089	−0.60–−0.56	4.67 ± 0.35
0.18–0.20	29.4 ± 1.2	1.8–2.0	1.475 ± 0.083	−0.56–−0.52	4.74 ± 0.32
0.20–0.22	26.9 ± 1.1	2.0–2.2	1.246 ± 0.077	−0.52–−0.48	4.82 ± 0.30
0.22–0.24	24.8 ± 1.0	2.2–2.4	1.338 ± 0.080	−0.48–−0.44	4.92 ± 0.28
0.24–0.26	26.6 ± 1.0	2.4–2.6	1.048 ± 0.071	−0.44–−0.40	4.60 ± 0.26
0.26–0.28	22.15 ± 0.90	2.6–2.8	0.823 ± 0.063	−0.40–−0.36	4.79 ± 0.25
0.28–0.30	19.07 ± 0.82	2.8–3.0	0.947 ± 0.068	−0.36–−0.32	5.38 ± 0.26
0.30–0.32	19.04 ± 0.82	3.0–3.2	0.937 ± 0.067	−0.32–−0.28	4.84 ± 0.24
0.32–0.34	16.40 ± 0.75	3.2–3.4	0.634 ± 0.056	−0.28–−0.24	4.55 ± 0.23
0.34–0.36	16.16 ± 0.75	3.4–3.6	0.632 ± 0.056	−0.24–−0.20	4.57 ± 0.23
0.36–0.38	14.53 ± 0.71	3.6–3.8	0.639 ± 0.056	−0.20–−0.16	4.50 ± 0.22
0.38–0.40	13.35 ± 0.68	3.8–4.0	0.543 ± 0.052	−0.16–−0.12	4.69 ± 0.23
0.40–0.42	12.26 ± 0.66	4.0–4.2	0.456 ± 0.048	−0.12–−0.08	4.40 ± 0.22
0.42–0.44	11.83 ± 0.65	4.2–4.4	0.418 ± 0.046	−0.08–−0.04	4.81 ± 0.23
0.44–0.46	10.42 ± 0.61	4.4–4.6	0.414 ± 0.045	−0.04–0.00	4.65 ± 0.23
0.46–0.48	8.64 ± 0.56	4.6–4.8	0.375 ± 0.043	0.00–0.04	4.65 ± 0.23
0.48–0.50	7.76 ± 0.54	4.8–5.0	0.341 ± 0.041	0.04–0.08	4.40 ± 0.23
0.50–0.52	7.43 ± 0.54	5.0–5.2	0.297 ± 0.039	0.08–0.12	4.45 ± 0.23
0.52–0.54	7.07 ± 0.53	5.2–5.4	0.237 ± 0.035	0.12–0.16	4.75 ± 0.25
0.54–0.56	5.70 ± 0.49	5.4–5.6	0.268 ± 0.037	0.16–0.20	4.38 ± 0.24
0.56–0.58	5.20 ± 0.48	5.6–5.8	0.213 ± 0.033	0.20–0.24	4.67 ± 0.26
0.58–0.60	4.56 ± 0.46	5.8–6.0	0.183 ± 0.030	0.24–0.28	4.27 ± 0.25
0.60–0.62	4.13 ± 0.45	6.0–6.2	0.153 ± 0.028	0.28–0.32	4.72 ± 0.28
0.62–0.64	3.81 ± 0.45	6.2–6.4	0.173 ± 0.030	0.32–0.36	4.51 ± 0.02
0.64–0.66	3.74 ± 0.46	6.4–6.6	0.128 ± 0.026	0.36–0.40	4.79 ± 0.30
0.66–0.68	2.06 ± 0.35	6.6–6.8	0.194 ± 0.032	0.40–0.44	4.52 ± 0.31
0.68–0.70	1.93 ± 0.35	6.8–7.0	0.143 ± 0.027	0.44–0.48	5.14 ± 0.35
0.70–0.72	2.42 ± 0.40	7.0–7.2	0.113 ± 0.024	0.48–0.52	4.10 ± 0.34
0.72–0.74	1.81 ± 0.35	7.2–7.4	0.133 ± 0.026	0.52–0.56	4.34 ± 0.38
0.74–0.76	1.13 ± 0.29	7.4–7.6	0.087 ± 0.021	0.56–0.60	5.06 ± 0.45
0.76–0.78	1.26 ± 0.32	7.6–7.8	0.118 ± 0.025	0.60–0.64	4.14 ± 0.45
0.78–0.80	0.84 ± 0.28	7.8–8.0	0.087 ± 0.021	0.64–0.68	3.97 ± 0.51
		8.0–8.2	0.113 ± 0.024	0.68–0.80	5.25 ± 0.79
		8.2–8.4	0.072 ± 0.019		
		8.4–8.6	0.051 ± 0.016		
		8.6–8.8	0.062 ± 0.018		
		8.8–9.0	0.077 ± 0.020		
		9.0–9.2	0.036 ± 0.014		
		9.2–9.4	0.061 ± 0.018		
		9.4–9.6	0.051 ± 0.016		
		9.6–9.8	0.026 ± 0.011		
		9.8–10.0	0.041 ± 0.014		

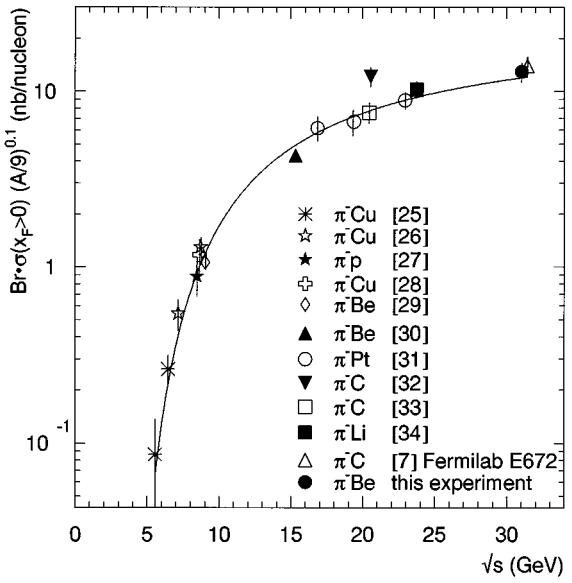

FIG. 10. Dependence of the product $B\sigma_{J/\psi}$ for $x_F>0$ on $\sqrt{s}$ for π^--nucleon interactions (uncertainties are statistical and systematic errors added in quadrature). Measurements from different targets have been normalized to Be assuming an $A^{0.9}$ atomic mass dependence. The curve represents the parametrization described in the text. Results from previous experiments have been adjusted to account for the appropriate $J/\psi\to\mu^+\mu^-$ branching ratio where necessary.

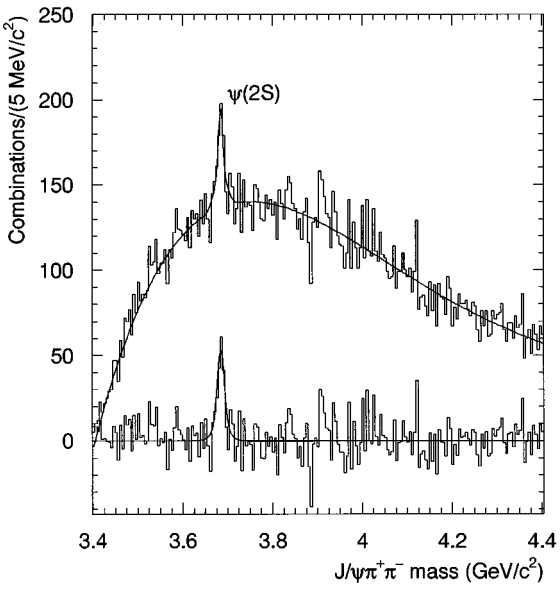

FIG. 11. The $J/\psi\pi^+\pi^-$ invariant mass distribution. The solid curve shows the fit to the data described in the text. The lower histogram shows the background-subtracted signal with the Monte Carlo expectation superimposed (solid curve).

dependence of the J/ψ cross section on $\sqrt{s}$ for $x_F>0$ is shown in Fig. 10. The effect of the different target materials used by the various experiments was accounted for by normalizing all data to beryllium, assuming an A^α atomic mass dependence, where $\alpha=0.90\pm0.02$ [1,7,15]. The curve in Fig. 10 represents a parametrization of the $\sqrt{s}$ dependence of the J/ψ production cross section in the form

$$\sigma=\sigma_0(1-M_{J/\psi}/\sqrt{s})^n, \tag{5.2}$$

with $\sigma_0=(25.7\pm1.9)$ nb/nucleon and $n=7.3\pm0.26$.

VI. $\psi(2S)$ PRODUCTION

We have detected $\psi(2S)$'s both in the dimuon (Fig. 4) and in the $J/\psi\pi^+\pi^-$ (Fig. 11) decay modes. We report on (i) differential and integrated $\psi(2S)$ cross sections, (ii) the fraction of inclusive J/ψ's due to $\psi(2S)$ decays, and (iii) the ratio of the $\psi(2S)$ decay rates into $J/\psi\pi^+\pi^-$ and $\mu^+\mu^-$.

For the analysis of $J/\psi\pi^+\pi^-$ final states, we used the J/ψ four-momenta combined with the four-momenta of two opposite-sign charged tracks (assumed to be pions) originating from the same primary vertex. The $J/\psi\pi^+\pi^-$ mass was calculated by adding the nominal J/ψ mass to the difference between the invariant masses of the $\mu^+\mu^-\pi^+\pi^-$ and $\mu^+\mu^-$ systems. Tracks identified either as muons (via penetration through the muon detector), or as electrons from photon conversions (via detection of pairs of opposite charge tracks with an invariant mass less than 20 MeV/c^2), were not considered as candidate pion tracks. We also required the ratio of invariant masses, $R_{\pi\pi}=M_{\pi\pi}/(M_{\mu\mu\pi\pi}-M_{\mu\mu})$, to be greater than 0.8. This requirement was imposed since, according to Brown and Cahn [16], the phase space for a decay such as $\psi(2S)\to J/\psi\pi^+\pi^-$ is modified by chiral symmetry so that the dipion mass distribution is skewed toward high values, a conjecture strongly supported by Mark III data [17]. Our data, shown in Fig. 12, are also consistent with the $R_{\pi\pi}$ distribution measured by Mark III. Requiring $R_{\pi\pi}>0.8$ reduced the number of combinations by a factor of 4 with an estimated 23% loss of $\psi(2S)$ signal.

The resulting $J/\psi\pi^+\pi^-$ mass plot, shown in Fig. 11, exhibits a clear $\psi(2S)$ signal with a FWHM of 12 MeV/c^2, consistent with our Monte Carlo simulation. A fit to the

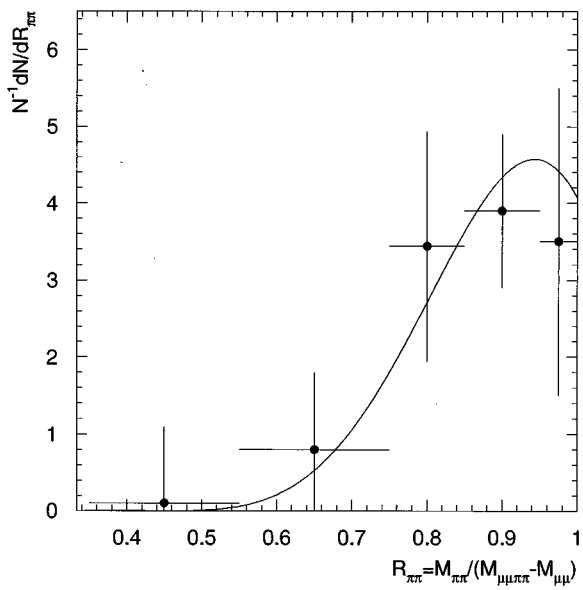

FIG. 12. The distribution of $R_{\pi\pi}$ for $\psi(2S)\to J/\psi\pi^+\pi^-$ decays. The points represent our background-subtracted data; the curve represents the parametrization of the Mark III results [17].

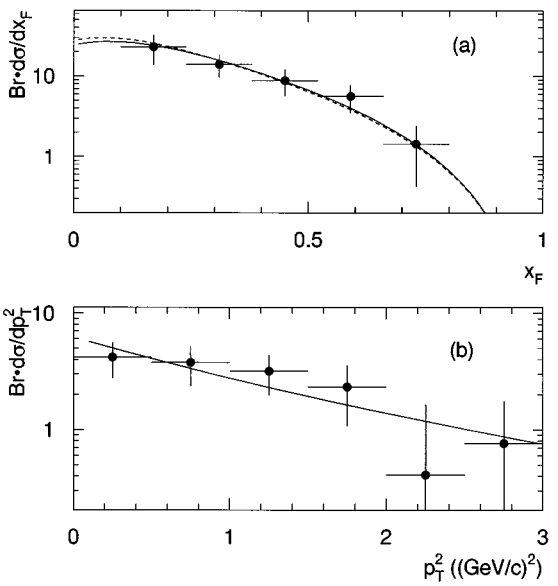

FIG. 13. Product of $B(\psi(2S)\rightarrow J/\psi\pi^+\pi^-)$ and $\psi(2S)$ differential cross section as a function of (a) x_F (nb/nucleon), (b) p_T^2 [nb/nucleon/(GeV/c)^2]. The solid curves are the parametrizations given by Eqs. (4.1)–(4.3) using the values of the parameters determined by fits for J/ψ production, and substituting the $\psi(2S)$ mass in the τ calculation. The shape of the fitted inclusive $J/\psi x_F$ distribution is shown as a dashed curve in (a) for comparison. The curves are normalized to the $\psi(2S)$ branching ratio times the inclusive cross section.

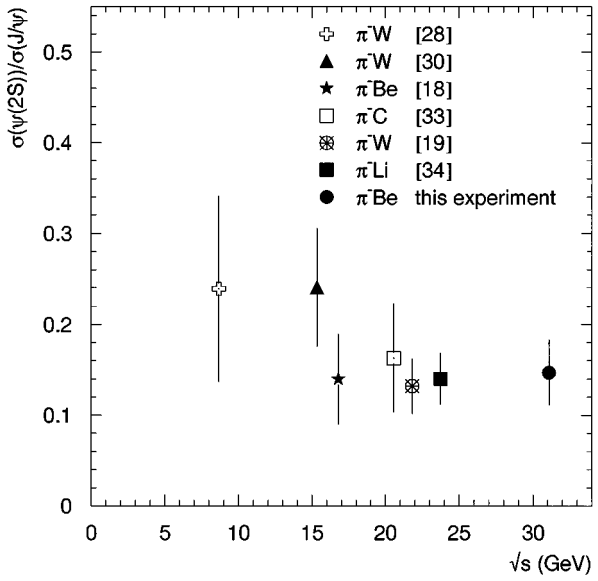

FIG. 14. Dependence of the ratio of inclusive $\psi(2S)$ and J/ψ cross sections on $\sqrt{s}$ for π^--nucleon interactions (uncertainties are statistical and systematic errors added in quadrature).

$J/\psi\pi^+\pi^-$ mass spectrum using a two-Gaussian resolution function for the signal and a fifth-order polynomial for the background yields 224 ± 44(stat)±20(syst) background-subtracted combinations. The $\psi(2S)$ mass obtained from the fit is (3.684 ± 0.002) GeV/c^2. The systematic error in the number of $\psi(2S)$ combinations reflects the uncertainties in the background and signal shapes.

The $\psi(2S)$ differential cross section as a function of x_F and p_T^2 is shown in Fig. 13 and tabulated in Table II. These distributions were obtained by fitting the $J/\psi\pi^+\pi^-$ mass spectrum in bins of x_F and p_T^2. The resulting background-subtracted signals in each bin were corrected for acceptance and reconstruction efficiency, including the effects of the $R_{\pi\pi}$ requirement. The differential distributions were normalized to the branching ratio times the measured integrated cross section (discussed below). Other measurements of the

TABLE II. Differential cross sections for $\psi(2S)$ production in 515 GeV/c π^-Be interactions. Quoted uncertainties reflect statistical errors only. The normalization uncertainty is $\pm16\%$.

x_F bin	$d\sigma/dx_F$ (nb/nucleon)	p_T^2 bin [(GeV/c)^2]	$d\sigma/dp_T^2$ [nb/nucleon/(GeV/c)^2]
		0.0–0.5	4.2 ± 1.4
0.10–0.24	23.1 ± 9.3	0.5–1.0	3.8 ± 1.4
0.24–0.38	13.9 ± 4.4	1.0–1.5	3.2 ± 1.2
0.38–0.52	8.8 ± 3.2	1.5–2.0	2.4 ± 1.3
0.52–0.66	5.6 ± 2.1	2.0–2.5	0.4 ± 1.2
0.66–0.80	1.4 ± 1.0	2.5–3.0	0.8 ± 1.0

$\psi(2S)$ differential cross section have employed the dimuon decay mode using 150 GeV/c [18] and 253 GeV/c [19] incident pions, and 800 GeV/c incident protons in the central x_F region [20].

The solid curves in Fig. 13 represent the parametrizations given by Eqs. (4.1)–(4.3) with the $\psi(2S)$ mass substituted for the J/ψ mass, and the values for a,κ,β,c from the fit to the J/ψ differential spectra reported in Sec. IV. The observed agreement demonstrates that the shapes of the measured J/ψ and $\psi(2S)$ differential distributions can be described by similar parametrizations. We use these parametrizations in the evaluation of acceptance and efficiency in the following $\psi(2S)$ analyses.

Based on a signal of 224 ± 44(stat)±20(syst) detected $\psi(2S)$'s, we obtain $B(\psi(2S)\rightarrow J/\psi\pi^+\pi^-)\sigma(\pi^-\text{Be}\rightarrow\psi(2S)+X)/A=[7.4\pm1.5(\text{stat})\pm1.2(\text{syst})]$ nb/nucleon for $x_F>0.1$. The systematic uncertainty quoted assumes the J/ψ and $\psi(2S)$ x_F distributions are described by the same parametrization, and takes into account variation in the measured $J/\psi x_F$ distribution [a variation of ±0.4 in the value of $\kappa=2.2$ in Eq. (4.1)]. It does not account for possible contributions due to the $R_{\pi\pi}$ requirement.

Using the branching ratios $B(J/\psi\rightarrow\mu^+\mu^-)=0.0597\pm0.0025$ and $B(\psi(2S)\rightarrow J/\psi\pi^+\pi^-)=0.324\pm0.026$ [10], the ratio of the inclusive cross sections, $\sigma(\pi^-\text{Be}\rightarrow\psi(2S)+X)/\sigma(\pi^-\text{Be}\rightarrow J/\psi+X)$, is 0.15 ± 0.03(stat) ±0.02(syst). This ratio is consistent with results obtained at lower energies, as shown in Fig. 14, and exhibits little variation over the $\sqrt{s}$ range currently accessible.

The fractional contribution of all $\psi(2S)$ decays to the observed J/ψ signal is given by

$$f_{\psi(2S)}=\frac{N'_{\psi(2S)\rightarrow J/\psi\pi^+\pi^-}\times B(\psi(2S)\rightarrow J/\psi X)}{N_{J/\psi\rightarrow\mu^+\mu^-}\times B(\psi(2S)\rightarrow J/\psi\pi^+\pi^-)}k_1, \tag{6.1}$$

where $B(\psi(2S)\to J/\psi X)=0.57\pm0.04$ [10]. $N_{J/\psi\to\mu^+\mu^-}=9600\pm105(\text{stat})\pm100(\text{syst})$ is the number of J/ψ's having x_F in the range 0.1–0.8, $N'_{\psi(2S)\to J/\psi\pi^+\pi^-}=220\pm44(\text{stat})\pm20(\text{syst})$ is the number of $\psi(2S)$'s that decay into a J/ψ in the same x_F range. The factor k_1 represents the relative detection efficiency (product of acceptance and reconstruction efficiency) of the J/ψ and $\psi(2S)$ decay modes:

$$k_1=\frac{a_{J/\psi\to\mu^+\mu^-}\cdot\varepsilon_{J/\psi\to\mu^+\mu^-}}{a_{\psi(2S)\to J/\psi\pi^+\pi^-}\cdot\varepsilon_{\psi(2S)\to J/\psi\pi^+\pi^-}}=2.07\pm0.12(\text{syst}). \tag{6.2}$$

Using the above values, we find $f_{\psi(2S)}=0.083\pm0.017(\text{stat})\pm0.013(\text{syst})$ in the J/ψ x_F range 0.1–0.8. The systematic uncertainty quoted also does not account for uncertainties due to the $R_{\pi\pi}$ requirement. This is the first determination of $f_{\psi(2S)}$ using $\psi(2S)$ decays into J/ψ; previous measurements used the $\mu^+\mu^-$ decay mode of the $\psi(2S)$ [21–23]. Our value for $f_{\psi(2S)}$ is consistent with these measurements.

The ratio of the $\psi(2S)$ decay partial widths was determined as

$$\frac{B(\psi(2S)\to J/\psi\pi^+\pi^-)}{B(\psi(2S)\to\mu^+\mu^-)}=\frac{N_{\psi(2S)\to J/\psi\pi^+\pi^-}}{N_{\psi(2S)\to\mu^+\mu^-}\times B(J/\psi\to\mu^+\mu^-)}k_2, \tag{6.3}$$

where $N_{\psi(2S)\to J/\psi\pi^+\pi^-}=224\pm44(\text{stat})\pm20(\text{syst})$ and $N_{\psi(2S)\to\mu^+\mu^-}=270\pm35(\text{stat})\pm50(\text{syst})$, and $k_2=2.17\pm0.17(\text{syst})$ is the ratio of the detection efficiencies in the two modes. We find $B(\psi(2S)\to J/\psi\pi^+\pi^-)/B(\psi(2S)\to\mu^+\mu^-)=30.2\pm7.1(\text{stat})\pm6.8(\text{syst})$ (again, the systematic uncertainty quoted does not include contributions due to the $R_{\pi\pi}$ requirement). The current world average for this ratio calculated from Particle Data Group information is 42 ± 10 [10].

VII. SEARCH FOR ''HIDDEN'' CHARM RESONANCE STATES

We searched for evidence of the enhancement in the $J/\psi\pi^+\pi^-$ mass spectrum around 3.836 GeV/c^2 reported in [24]. A fit to the mass spectrum obtained in the $\psi(2S)$ analysis (see Sec. VI) was performed using a double-Gaussian resolution function centered at 3.836 GeV/c^2 for the ''hidden'' charm candidate, in addition to $\psi(2S)$ and background shapes. Figure 15(a) shows the result of this fit. The excess was calculated as the number of entries above the fitted background in the mass region (3.836 ± 0.015) GeV/c^2. This procedure yields $52\pm30(\text{stat})$ background-subtracted combinations to be compared with $224\pm44(\text{stat})$ $\psi(2S)$ combinations. The corresponding 90% confidence level upper limit on the value for $B(X(3836)\to J/\psi\pi^+\pi^-)\sigma(\pi^-\text{Be}\to X(3836)+X)/A$ for $x_F>0.1$ is 3.1 nb/nucleon, assuming the same production properties for the $\psi(2S)$ and the ''hidden'' charm resonance. The 90% confidence level upper limit is the cross section calculated for the (statistically insignificant) number of background-subtracted combinations observed plus 1.28 times the sum in quadrature of the statistical uncertainty and a 20% systematic uncertainty.

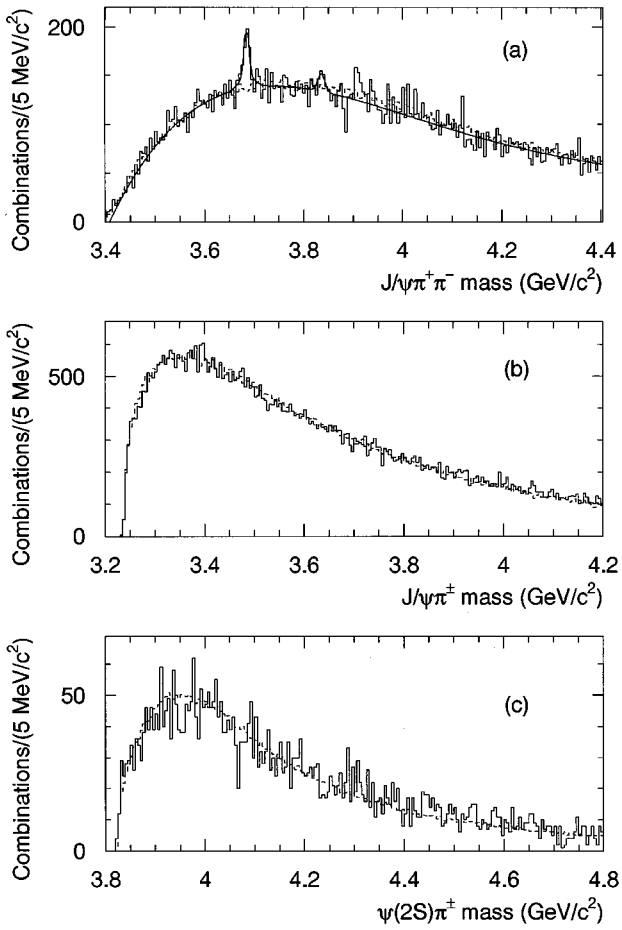

FIG. 15. The invariant mass distributions for (a) $J/\psi\pi^+\pi^-$, (b) $J/\psi\pi^\pm$, and (c) $\psi(2S)\pi^\pm$ combinations. The solid curve in (a) represents a fit to the candidate ''hidden'' charm resonance plus background as described in the text. Dashed histograms show the mass spectra obtained by combining J/ψ or $\psi(2S)$ candidates and pions from different events.

We have also investigated $J/\psi\pi^\pm$ and $\psi(2S)\pi^\pm$ spectra in a search for charged resonance states decaying into either J/ψ or $\psi(2S)$, plus a single charged pion. The search involving the $\psi(2S)$ employed $\psi(2S)\to J/\psi\pi^+\pi^-$ events. As shown in Figs. 15(b) and 15(c), the data indicate no evidence for significant structure. Mass spectra obtained by combining J/ψ or $\psi(2S)$ and pions from different events are also shown for comparison.

VIII. SUMMARY

We have studied the production of J/ψ and $\psi(2S)$ charmonium mesons in 515 GeV/c π^- Be collisions in the Feynman-x range $0.1<x_F>0.8$. For $x_F>0.1$, we measure the cross sections $B(J/\psi\to\mu^+\mu^-)\sigma(\pi^-\text{Be}\to J/\psi+X)/A=[9.3\pm0.1(\text{stat})\pm1.1(\text{syst})]$ nb/nucleon and $B(\psi(2S)\to J/\psi\pi^+\pi^-)\sigma(\pi^-\text{Be}\to\psi(2S)+X)/A=[7.4\pm1.5(\text{stat})\pm1.2(\text{syst})]$ nb/nucleon. The shapes of the measured differential distributions for the J/ψ and $\psi(2S)$ can be adequately described by the same parametrization.

The fraction of the inclusive J/ψ yield due to $\psi(2S)$ decays is $f_{\psi(2S)}=0.083\pm0.017(\text{stat})\pm0.013(\text{syst})$. The ra-

tio of two $\psi(2S)$ decay rates $B(\psi(2S)\to J/\psi\pi^+\pi^-)/B(\psi(2S)\to\mu^+\mu^-)$ is $30.2\pm7.1(\text{stat})\pm6.8(\text{syst})$.

We have also searched for production of ''hidden'' charm resonances decaying into either $J/\psi\pi^\pm, \psi(2S)\pi^\pm$, or $J/\psi\pi^+\pi^-$ systems. We find no statistically significant evidence for the recently reported enhancement at a $J/\psi\pi^+\pi^-$ mass of 3.836 GeV/c^2.

ACKNOWLEDGMENTS

We thank the staffs of all the participating institutions, especially those of Fermilab and the Institute for High Energy Physics (IHEP) at Protvino. This work was supported by the U. S. Department of Energy, the National Science Foundation, and the Russian Ministries of Science and Atomic Energy.

[1] G. A. Schuler, ''Quarkonium Production and Decays,'' CERN Report No. CERN-TH.7170/94, 1994 (unpublished).

[2] M. Vanttinen, P. Hoyer, S. J. Brodsky, and W. -K. Tang, Phys. Rev. D **51**, 3332 (1995).

[3] V. Koreshev *et al.* (in preparation).

[4] E. Engels, Jr. *et al.*, Nucl. Instrum. Methods A **279**, 272 (1989).

[5] C. Bromberg *et al.*, Nucl. Instrum. Methods A **307**, 292 (1991).

[6] F. Lobkowicz *et al.*, Nucl. Instrum. Methods A **235**, 332 (1985); G. Alverson *et al.*, Phys. Rev. D **48**, 5 (1993).

[7] S. Kartik *et al.*, Phys. Rev. D **41**, 1 (1990).

[8] V. Abramov *et al.*, ''Properties of J/ψ Production in π^- Be and p-Be Collisions at 530 GeV/c,'' Fermilab Report No. FERMILAB-Pub-91/62-E, 1991 (unpublished).

[9] R. R. Crittenden *et al.*, Nucl. Instrum. Methods A **270**, 99 (1988).

[10] Particle Data Group, L. Montanet *et al.*, Phys. Rev. D **50**, 1173 (1994).

[11] V. G. Kartvelishvili and A. K. Likhoded, Sov. J. Nucl. Phys. **39**, 298 (1984).

[12] D. M. Kaplan *et al.*, Phys. Rev. Lett. **40**, 435 (1978).

[13] The cross sections quoted in [8] must be increased by a factor 1.2 to account for a correction omitted in the luminosity calculations.

[14] Note that the measurement of the integrated J/ψ cross section reported in R. Jesik *et al.*, Phys. Rev. Lett. **74**, 495 (1995), is not independent since it is based upon an analysis of data from the sample discussed in this paper.

[15] D. M. Alde *et al.*, Phys. Rev. Lett. **66**, 133 (1991).

[16] L. S. Brown and R. N. Cahn, Phys. Rev. Lett. **35**, 1 (1975).

[17] D. Coffman *et al.*, Phys. Rev. Lett. **68**, 282 (1992).

[18] M. A. Abolins *et al.*, Phys. Lett. **82B**, 145 (1979).

[19] J. G. Heinrich *et al.*, Phys. Rev. D **44**, 1909 (1991).

[20] T. Alexopoulos *et al.*, *in Proceedings of the 27th International Conference on High Energy Physics*, Glasgow, Scotland, 1994, edited by P. J. Bussey and I. G. Knowles (IOP, London, 1995); M. H. Schub *et al.*, Phys. Rev. D **52**, 1307 (1995).

[21] J. G. McEwen *et al.*, Phys. Lett. **121B**, 198 (1983).

[22] S. R. Hahn *et al.*, Phys. Rev. D **30**, 671 (1984).

[23] L. Antoniazzi *et al.*, Phys. Rev. Lett. **70**, 383 (1993).

[24] L. Antoniazzi *et al.*, Phys. Rev. D **50**, 4258 (1994).

[25] J. Alspector *et al.*, Phys. Lett. **81B**, 397 (1979); J. LeBritton *et al.*, *ibid.* **81B**, 401 (1979).

[26] Yu. B. Bushnin *et al.*, Phys. Lett. **72B**, 269 (1977).

[27] F. Binon *et al.*, Nucl. Phys. **B239**, 311 (1984).

[28] M. J. Corden *et al.*, Phys. Lett. **68B**, 96 (1977); **96B**, 411 (1980).

[29] Yu. M. Antipov *et al.*, Phys. Lett. **72B**, 278 (1977).

[30] S. Katsanevas *et al.*, Phys. Rev. Lett. **60**, 2121 (1988); C. Akerlof *et al.*, Phys. Rev. D **48**, 5067 (1993).

[31] J. Badier *et al.*, Z. Phys. C **20**, 101 (1983).

[32] J. G. Branson *et al.*, Phys. Rev. Lett. **38**, 1331 (1977).

[33] K. J. Anderson *et al.*, Phys. Rev. Lett. **42**, 944 (1979).

[34] L. Antoniazzi *et al.*, Phys. Rev. D **46**, 4828 (1992).